JOURNAL OF AIRCRAFT
Vol. 44, No. 4, July–August 2007

Plasma Actuators for Hingeless Aerodynamic Control of an Unmanned Air Vehicle

Mehul P. Patel,* T. Terry Ng,† and Srikanth Vasudevan‡
Orbital Research Inc., Cleveland, Ohio 44103
and
Thomas C. Corke§ and Chuan He¶
University of Notre Dame, Notre Dame, Indiana 46556

DOI: 10.2514/1.25368

The use of dielectric barrier discharge plasma actuators for hingeless flow control over a 47-deg 1303 unmanned combat air vehicle wing is described. Control was implemented at the wing leading edge to provide longitudinal control without the use of hinged control surfaces. Wind-tunnel tests were conducted at a chord Reynolds number of 4.12×10^5 and angles of attack ranging from 15 to 35 deg to evaluate the performance of leading-edge plasma actuators for hingeless flow control. Operated in an unsteady mode, the actuators were used to alter the flowfield over the lee-side wing to modify the aerodynamic lift and drag forces on the vehicle. Multiple configurations of the plasma actuator were tested on the lee side and wind side of the wing leading edge to affect the wing aerodynamics. Data acquisition included force-balance measurements, laser fluorescence, and surface flow visualizations. Flow visualization tests mainly focused on understanding the vortex phenomena over the baseline uncontrolled wing to aid in identifying optimal locations for plasma actuators for effective flow manipulation. Force-balance results show considerable changes in the lift and drag characteristics of the wing for the plasma-controlled cases compared with the baseline cases. When compared with the conventional traditional trailing-edge devices, the plasma actuators demonstrate a significant improvement in the control authority in the 15- to 35-deg angle-of-attack range, thereby extending the operational flight envelope of the wing. The study demonstrates the technical feasibility of a plasma wing concept for hingeless flight control of air vehicles, in particular, vehicles with highly swept wings and at high angles of attack flight conditions in which conventional flaps and ailerons are ineffective.

Nomenclature

α	=	angle of attack, deg
b	=	wing span, m
C_D	=	drag coefficient
C_L	=	lift coefficient
c	=	mean aerodynamic chord, m
F^+	=	nondimensional frequency of the actuator
f_{mod}	=	modulation frequency, Hz
L_{sep}	=	streamwise extent of the separation zone, m
Re_c	=	Reynolds number based on the mean chord and freestream velocity
St	=	Strouhal number based on the mean chord
U_∞	=	freestream velocity at the entrance to the test section, m/s
x	=	distance from the leading edge, m
y	=	spanwise distance from the centerline, m

I. Introduction

TECHNOLOGIES that broaden the roles and capabilities of unmanned air vehicles (UAVs) are of significant interest to the aerospace community. This is due to a sharp rise in the demand and applications for UAVs for both military and civilian operations. Active flow control is one such technology that holds considerable promise in advancing the aerodynamic performance and maneuvering of UAVs. The technology is based on the use of small-scale actuators that elicit desired changes in the flow state by altering the balance of flowfield energy using flow-manipulation methods. This allows for elimination or reduction of traditional control surfaces and other variable geometry for aerodynamic control. It can also be used to enhance the performance of traditional control surfaces or the operational flight envelope of air vehicles by providing controls at flight conditions in which conventional control surfaces are ineffective. The actuators can be passive or active and can be operated in an open-loop or closed-loop fashion, as desired for the given application. Flow control has been shown to control or promote boundary-layer transition, augment lift, reduce drag, or modify acoustic emissions [1].

The quest for efficient flow control for improved vehicle aerodynamics has led to the development of many ingenious actuators and control techniques over the years [1]. Examples of flow control include passive and active vortex generators [1,2], suction [3], blowing [4], oscillatory blowing/suction [5], synthetic jet actuators [6], and dielectric barrier discharge (DBD) plasma actuators [7], to name a few. Although there are a number of different types of flow control actuators, it is becoming increasingly clear that for an actuator to buy its way onto an air vehicle, it not only needs to demonstrate the ability to generate the forces necessary for control, but also an overall improvement in the aerodynamic and structural efficiencies of the vehicle, relative to the conventional control system. The DBD plasma actuator has received considerable attention over the recent years as a practical flow control device due to its simple lightweight design with no moving parts, low energy consumption, and because of its ability to generate momentum without the need for fluidic plumbing.

There is a large body of work on the use of different plasma generation methods for flow control, including dc glow discharge, RF glow discharge, and dielectric barrier discharge [8]. The DBD

Received 17 July 2006; revision received 26 April 2007; accepted for publication 27 April 2007. Copyright © 2007 by M. Patel and T. Corke. Published by the American Institute of Aeronautics and Astronautics, Inc., with permission. Copies of this paper may be made for personal or internal use, on condition that the copier pay the $10.00 per-copy fee to the Copyright Clearance Center, Inc., 222 Rosewood Drive, Danvers, MA 01923; include the code 0021-8669/07 $10.00 in correspondence with the CCC.

*Director, Aerodynamics Group, 4415 Euclid Avenue, Suite 500. Senior Member AIAA.
†Chief Aerodynamicist, 4415 Euclid Avenue, Suite 500. Senior Member AIAA.
‡Aerospace Engineer, 4415 Euclid Avenue, Suite 500. Member AIAA.
§Clark Chair Professor, Aerospace and Mechanical Engineering Department, 101 Hessert Laboratory for Aerospace Research. Associate Fellow AIAA.
¶Ph.D. Candidate, Aerospace and Mechanical Engineering Department, 101 Hessert Laboratory for Aerospace Research.

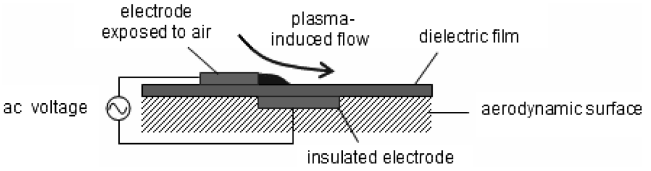

Fig. 1 Schematic of a DBD plasma actuator showing asymmetric electrode arrangement, dielectric layer, and location of plasma formation. The actuator location is referenced to the junction of the exposed and covered electrodes.

plasma actuator, the actuator used in the present study, consists of two electrodes that are separated by a dielectric material. One of the electrodes is typically exposed to the surrounding air and the other is fully encapsulated by a dielectric material. Figure 1 shows a schematic illustration of the electrode configuration for the DBD plasma actuator. When an ac voltage (5 kHz) is supplied to the electrodes at sufficiently high amplitude levels (3–12 kV peak to peak), the air ionizes in the region of the largest electric field potential. This typically occurs at the edge of the electrode that is exposed to the air and spreads out over the area projected by the covered electrode, directing momentum into the surrounding air. The process of ionizing the air in this configuration is classically known as a dielectric barrier discharge [9].

The basis of the DBD plasma actuator configuration is that the ionized air (plasma) in the presence of an electric field gradient produces a body force on the ambient air [10], which induces a virtual aerodynamic shape over the surface around the actuator. The body-force vector can be tailored for a given application by configuring the orientation and design of the electrode geometry. Enloe et al. [10] showed that the formation of the plasma is a dynamic process that varies in time and space during the ac cycle. Orlov et al. [11] recently developed a lumped circuit model from which the space–time-dependent body force can be computed. This model provides insight in the dependence of the body force on the ac frequency and amplitude, wave-form shape, and electrode geometry.

Plasma examples of flow control applications using the DBD plasma actuators include exciting three-dimensional boundary-layer instabilities on a sharp cone at Mach 3.5 [12], lift augmentation on wings [13], separation control for low-pressure turbine blades [14], leading-edge separation control on wing sections [15], phased plasma arrays for unsteady flow control [16], and control of the dynamic stall vortex on oscillating airfoils [17]. More recently, the use of plasma actuators has been demonstrated for air vehicle control through applications such as plasma flaps and slats [18], smart plasma slat [19], and plasma-optimized airfoil [20]. In the plasma slat application, Corke et al. [18] demonstrated the use of the plasma actuator on the leading edge of a two-dimensional NACA 0015 airfoil in a manner that mimics the effect of a movable leading-edge slat of a conventional high-lift system. In the smart plasma slat application by Patel et al. [19], the system presented in [18] was further developed to include closed-loop control using a single high-bandwidth pressure sensor and a feedback controller for autonomous sense and control of incipient flow separation and wing stall.

A majority of plasma flow control research to date has focused on controlling flow separation over two-dimensional geometries. These early studies clearly showed that plasma actuators could delay separation and increase the stall angle of attack and maximize lift coefficient of the lifting surfaces. Only recently have researchers been looking at applying plasma flow control to create aerodynamic control moments on air vehicle surfaces.

The present work explores the application of a DBD plasma actuator for controlling the longitudinal dynamics of a three-dimensional UCAV with a 47-deg leading-edge sweep. The UCAV configuration chosen for this study is based on a previously examined U.S. Air Force–Boeing 1303 UCAV design. Figure 2 shows the details of the 1303 UCAV wing used in this study. The vehicle is basically a blended wing body on which the fuselage is blended smoothly with the wing, with a varying cross-section along the span and ± 30- deg trailing-edge sweep angle. In its conventional configuration, the 1303 UCAV features movable flap and split ailerons at the trailing edge to control the vehicle. The goal of this research is to demonstrate the feasibility of a *plasma wing*: a flying wing that uses plasma flow control technology to create aerodynamic control moments of sufficient magnitude so that conventional moving aerodynamic controls could be eliminated. Because the 1303 UCAV contains a 47-deg leading-edge sweep, a discussion on the leading-edge vortex (LEV) is relevant to touch upon.

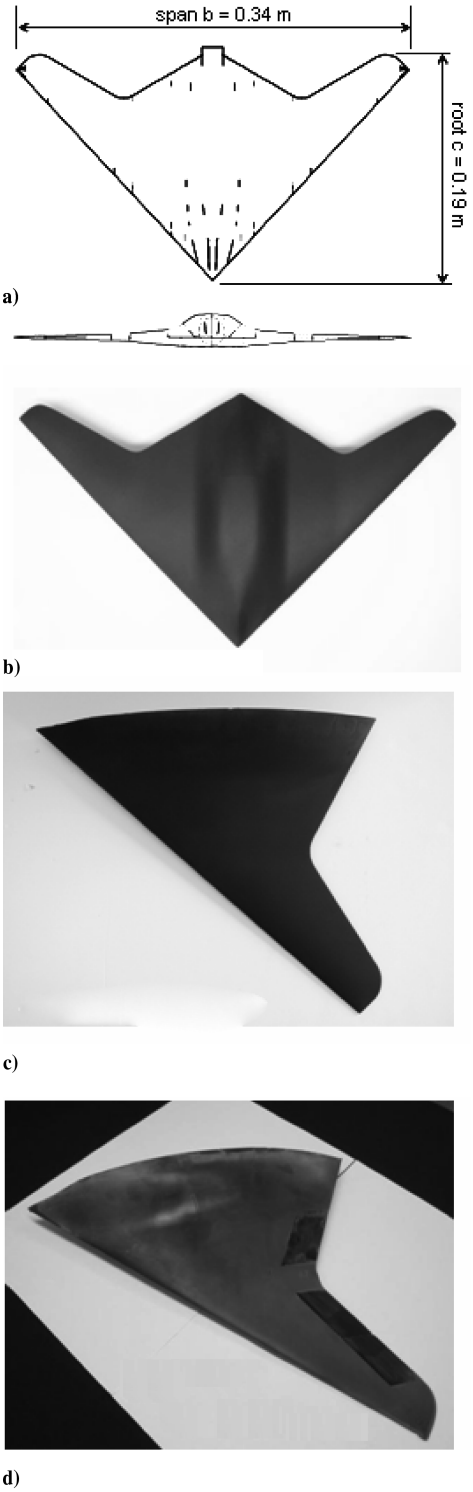

Fig. 2 The 1303 UCAV wing models used in the present study: a) a planform of the 2.31%-scale full-span wing model used for flow visualization studies, b) a photograph of the 2.31%-scale full-span wing model, c) a photograph of the 4.16%-scale half-span wing model used for plasma actuator experiments, and d) a photograph of the 4.16%-scale half-span wing model with conventional flap and split ailerons.

Swept wings of low aspect ratio are commonly used on high-speed aircraft because of their favorable wave-drag characteristics. The LEV is the main feature of the flow over swept wings that provide lift for flight control at high angles of attack. At low angles of attack and lower speeds, however, the aerodynamic behavior of swept wings is vastly different from that of the high-aspect ratio wings. The performance of swept wings outside the high-speed, high-alpha envelope is crucial, because the mission roles of modern aircraft require them to operate at low-speed and low-alpha conditions during different portions in flight (e.g., takeoff, landing, etc.). The formation of the LEV and subsequent vortex breakdown (VBD) phenomena over a swept wing are highly influenced by a number of parameters including angle of attack, leading-edge design, and adverse pressure gradients, which present unique challenges in controlling the vehicle dynamics at different flow conditions. For example, at low angles of attack, the flow remains attached to the surface and the location of the (weak) VBD is usually downstream within the wake of the wing. As the angle of attack increases, the strength of the LEV increases and the location of the VBD begins to move forward. The VBD phenomenon is usually associated with a loss in vortex lift, which has been shown to cause changes in the lift, drag, and pitching moments of the swept air vehicle [21–23]. At large angles of attack, the upper wing surfaces show the presence of complex vortex systems that dominate the leeward flowfield and cause the wingtip separations [24].

In the past decade, several researchers have employed flow control methods to control the LEV and VBD phenomena for improved aerodynamics of a swept wing. For example, Moeller and Rediniotis [25] demonstrated control of the pitching moment of a 60-deg swept-delta-wing model at high angles of attack using a series of surface-mounted pneumatic vortex control actuators. Control was achieved by altering the vortex breakdown phenomena that affected the chordwise lift distribution over the wing, ultimately resulting in an induced pitching moment. Amitay et al. [26] reported an experimental study on the use of synthetic jet actuators on a 1301 UCAV design (nicknamed Stingray). The design of Stingray [26] and the present 1303 UCAV share some similarity in that the leading-edge sweep angle is approximately 50 deg, leading to similar three-dimensional flow patterns over the wing. Amitay et al. [26] showed that at conditions in which the flow was normally separated from the leading edge, between 14- and 24-deg angles of attack, the zero-mass jets were able to produce significant forces and moments on the vehicle. Visser et al. [27–29] employed steady spanwise blowing to control leading-edge vortex breakdown and asymmetric roll-moment conditions.

In a more recent effort, a computational study on the aerodynamic performance of a 1303 UCAV design for different leading-edge designs was reported by Zhang et al. [30] The effects of three leading-edge designs [a basic profile, a rounded leading edge (similar to the one used in our study), and a sharp leading edge] were investigated using the NPARC code at a Mach number of 0.25 and at angles of attack ranging from $\alpha = -5$ to 20 deg. It was found that there were only minor differences among pressure distributions with the three configurations for both the computed and experimental data. The predicted pressure distributions compared favorably with the wind-tunnel measurements for all regions except near the wingtip, for which the computations did not consistently predict the separations. At small angles of attack, flowfield studies showed attached, smooth, and well-behaved flow.

In general, the flying wing aircraft that have been developed and successfully flown rely on multiple control surfaces distributed across the wing to provide control moments for trim and maneuvering. Each control surface is essentially a trailing-edge flap that when deflected, changes the lift, drag, and pitching moment over that portion of the wing. By suitably arranging multiple flaps across the wing, one can create moments to pitch, roll, or yaw the wing and moments to trim the wing at a particular flight condition. The ultimate objective of the present work is to demonstrate hingeless flight control with limited or no use of conventional control surfaces.

This paper presents results using plasma actuators placed near the leading edge to provide control at high-angle-of-attack ($\alpha = 15$ to 35 deg) flight conditions. The present work complements subsequent demonstrations on the 1303 UCAV planform for roll control using leading-edge plasma actuators [31] and for lift control at low angle of attack (α to 24 deg) using wind-side plasma actuators [32].

II. Experimental Setup

The UCAV planform used in this study is based on a 1303 design with varying cross sections, a 47-deg leading-edge sweep, and a ± 30-deg trailing-edge sweep (shown in Fig. 2a). The design was originally developed by the U.S. Air Force Research Laboratory (AFRL) in conjunction with Boeing Phantom Works and was recently used as a benchmark for a joint computational fluid dynamics code-validation effort by The Technical Cooperation Program (TTCP). TTCP involved a consortium of governmental interests in five countries to study the performance predictions of various Boeing/AFRL 1303 UCAV configurations with different leading edges [33–37]. In the present work, a 1303 configuration with a (relatively) blunt leading edge was used. The same configuration was later used in other plasma flow control demonstrations [31,32].

Photographs of the different full- and half-span models of the scaled 1303 UCAV used for wind-tunnel tests are shown in Figs. 2–4. Laser-smoke flow visualization experiments were conducted on a 2.31%-scale full-span model of the UCAV (shown in Fig. 2b), to capture off-surface flowfield information. Fluorescent-oil flow visualization and force-balance experiments were conducted on a 4.16%-scale, 0.4-m root chord, 0.34-m span, half-span model (shown in Fig. 2c). Tests were also conducted on a 4.16%-scale half-span model (shown in Fig. 2d) with traditional control surfaces, flap, and split ailerons, to quantify improvements in the overall control authority and the operational envelope of the wing using the plasma actuators. The half-span model has a root chord of 16 in. (40.64 cm) and a half-span dimension of 13.375 in. (13.97 cm). The models were cast from a numerically machined two-piece aluminum mold. The casting material was a mixture of epoxy and microglass beads that resulted in a very rigid model that accurately duplicated the mold shape.

Wind-tunnel experiments were conducted for angles of attack ranging from 0 to 35 deg. Many of the tests were performed from $\alpha = 0$ to 25 deg, however, additional tests were later conducted for angles of attack up to 35 deg. Lift and drag measurements on the half-span models were conducted in the 0.42 m (1.39 ft) square by 1.8 m (6 ft) long, cross-sectional, low-speed wind tunnel at the University of Notre Dame. All experiments were conducted at a chord Reynolds number Re_c of 4.12×10^5 based on the root chord, which corresponds to a Mach number of 0.045 and freestream velocity U_∞ of 15 m/s. The tunnel consists of a removable inlet with a series of 12 screens, followed by a 24:1 contraction that attaches to the test section. The turbulence level in the test section, u'/U_∞, was approximately 0.08%. The test section is equipped with a clear Plexiglas side wall that allows optical access to view the model. The back wall of the test section has removable panels that allow access into the test section.

The half-span models were mounted vertically on the support sting of a lift–drag force balance that was mounted on the top of the test section. The model was suspended below a splitter plate that was attached to the ceiling of the test section. The splitter plate was designed to produce a two-dimensional flow with a thin boundary layer leading up to the model. A hole in the ceiling splitter plate accommodated the sting supporting the model. Wiring for the plasma actuator also entered through this hole. This hole was aligned with the support sting so that it would not interfere with angular positioning of the model when setting different angles of attack. A stepper motor on the force balance drove the angular position of the support sting. Its motion was controlled by the data acquisition computer through software; with this, the angular position was repeatable to ± 0.005 deg.

The force balance consists of independent lift and drag platforms. The lift platform was supported on the drag platform by two vertical plates that flex only in the lift direction. The drag platform was

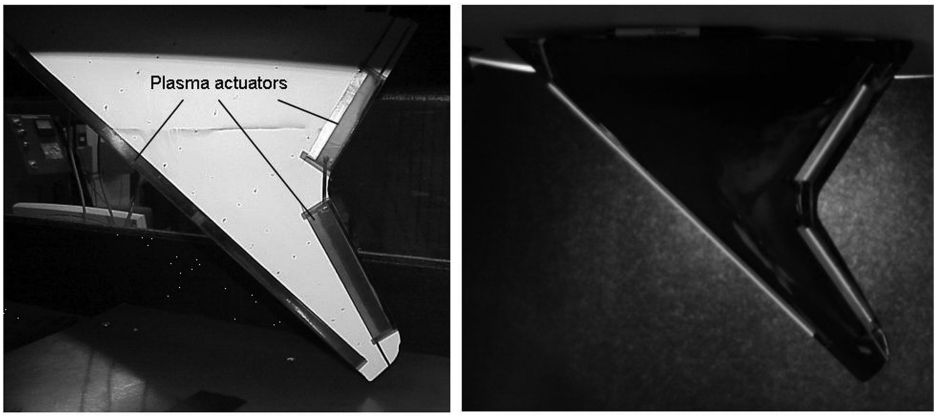

a) b)

Fig. 3 Photographs of a plasma wing model in a wind-tunnel test section (left), with plasma on (right).

supported by two plates that flex only in the drag direction and hang from two more vertical plates attached to the fixed base of the force balance. Both the lift and drag platforms were connected to separate flexures on which foil strain-gauge bridges were mounted. The strain-gauge bridges provided voltage outputs proportional to the respective lift and drag forces. The voltages were amplified using custom-designed operational amplifier circuits that minimized offset drift and sensitivity to external electronic noise. Calibration of the force balance was done by applying known weights to a cable pulley system attached to the support sting. The average uncertainty in the force measurements was 0.63% in lift and 0.9% in drag.

The experiment was controlled by a digital computer with a programmable analog-to-digital converter (ADC) and digital input–output (DIO) interface. The minimum voltage resolution of the ADC was 0.6 mV. The voltages proportional to the lift and drag forces were acquired along with a voltage proportional to the velocity at the entrance to the test section. The acquisition software was programmed to acquire 10,000 voltage samples over 10 s. This was found to provide repeatable time-averaged statistics that varied by less than 0.1%. The angular position of the airfoil was controlled by voltage pulses from the DIO into the stepper motor controller; with this, the angular position was repeatable to within ± 0.005 deg. A mechanical readout that was geared to the stepper motor shaft provided positive feedback on the angular position.

Before making lift–drag measurements, values of the lift and drag voltages were first acquired at different angles of attack without flow. Any difference from the zero-force voltage that was due to eccentric loading was recorded and subtracted from the results at the same angles of attack with flow. This process was repeated any time the model was removed from the force balance. The freestream speed at the entrance to the measurement section was measured with a pitot-static probe connected to a pressure transducer. The output of the transducer was monitored on a dc volt meter and simultaneously acquired by the data acquisition computer when the voltages proportional to the lift and drag forces were acquired. Based on the pressure transducer calibration, the accuracy of the freestream speed measurement was 0.01 m/s. The combination of the uncertainties in the force measurements and voltages resulted in an average uncertainty in the lift and drag coefficients of approximately 1%.

The high voltage leads to the plasma actuator were well shielded to minimize the noise effect, if any. The output from the lift and drag channels from the force balance were connected to an oscilloscope to check for RF noise interference when the plasma actuator is turned on. No noise interference was noticed on the scope. This confirmed that the plasma actuator did not corrupt the force data.

These experiments began with lift and drag measurements of the model with traditional control surfaces. Then fluorescent-oil flow visualization experiments were conducted that were used to characterize the vortex breakdown and separation lines at different angles of attack. Following this, laser-smoke flow visualization experiments were conducted to capture off-surface flowfield information on the lee side of the wing model. Finally, lift and drag measurements were performed on a half-span model to identify the optimal location for plasma actuators for lift control. These involved plasma actuators on the lee side and wind side of the wing leading edge.

In the present work, the plasma actuator consisted of two 0.05 mm (0.002 in.) thick copper electrodes separated by two layers of 0.05 mm (0.002 in.) thick Kapton film. The Kapton film has a breakdown voltage of approximately 7 kV per 10^{-3}-in. thickness and a dielectric constant of 3.3, which provide good electrical properties. The electrodes were arranged in an asymmetric arrangement, as shown in Fig. 1. They were overlapped by a small amount (on the order of 0.5 mm) to ensure a uniform plasma in the full spanwise direction. The plasma actuator was bonded directly to the surface of the wing. When the ac voltage amplitude was large enough, the air ionized in the region over the covered electrode. A 0.1-mm recess was molded into the wing model to secure the actuator flush to the surface. The two copper-foil electrodes were aligned parallel with the leading edge. The spanwise length of the actuators was 90% of the wing span. With this arrangement of electrodes, the body force produced by the actuator would induce a velocity component in the direction from the exposed electrode toward the covered electrode. With the actuator oriented on the leading edge, it induces a flow around the leading edge of the wing. Many different actuator arrangements were examined on both the lee-side and wind-side portions of the wing. Figure 3a shows an example of a plasma wing configuration examined with a continuous spanwise plasma actuator at the leading-edge and two trailing-edge split actuators. The effect of trailing-edge actuators are reported in a different study [32]. Figure 4 shows an example of a plasma wing configuration with multiple plasma actuators at the wing leading edge.

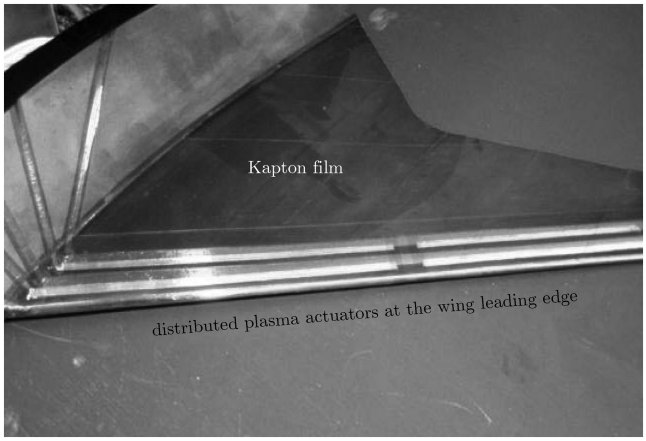

Fig. 4 Photograph of another plasma wing configuration with four actuators at the wing leading edge.

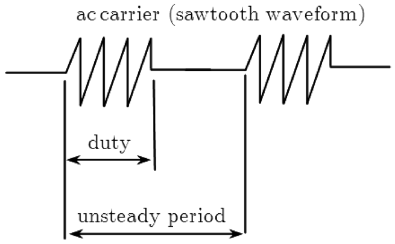

Fig. 5 Example of short-duty-cycle ac input for the unsteady operation of plasma actuators.

In all of the plasma control experiments presented here, the actuators were operated in an unsteady manner, as shown in Fig. 5. The ac carrier frequency supplied to the electrodes was 5 kHz and the ac voltage supplied to the electrodes was on the order of 3–12 kV_{p-p}. The power used by the actuator was approximately 2–4 W per linear foot of actuator span. In the unsteady mode, very short duty cycles are possible, which reduces the actuator power requirements significantly. For example, a 10% duty cycle provided results better than those of the steady operation, which used a 100% duty cycle. The unsteady actuator frequency f_{mod} was determined based on a Strouhal number St scaling of a dimensionless frequency, $F^+ = f_{\text{mod}}c/U_\infty = 1$, where f_{mod} is the modulation frequency, c is the mean aerodynamic chord, and U_∞ is the freestream velocity. Previous measurements [19] had shown that $F^+ = 1$ causes the optimum conditions to reattach separated leading-edge flows on wings. For all cases presented here, the unsteady modulation frequency of the actuator was $\sim$166 Hz and the actuator was operated at a 10% duty cycle.

III. Results

The results are presented in chronological order of the experiments, beginning with flow visualization that documents the basic features of the flow over the wing at different angles of attack. The flow visualization results guided the design and placement of the plasma actuators. The results of the lift–drag measurements with the plasma actuators documented the optimum arrangement to maximize the change in lift. The results presented here focus on the leading-edge actuators that were effective at larger angles of attack.

Figure 6 (left) shows a photograph of the wing trailing edge with conventional control surfaces, flap, and split ailerons. Figure 6 (right) shows a photograph of passive devices with 1-, 3-, and 5-deg deflections used in the wind-tunnel testing for the conventional control surfaces. The dimensions of the (inboard) flap and (outboard) split aileron (hereafter, aileron) are 0.1×0.04 m and 0.13×0.038 m, respectively, as shown in Fig. 2d. The effects of individual and combined deflection of the flap and aileron by 1, 3, and 5 deg on the lift forces of the wing were measured for $\alpha = 0$ to 25 deg with a 1-deg increment. These tests were conducted primarily to provide a basis for comparison with the plasma actuator effects, to highlight the inadequacy of 1303 conventional control surfaces in providing control at high angles of attack and, ultimately, to demonstrate improvements in control authority and the operational flight envelope of the wing using the plasma actuators. The results from these tests are highlighted in Fig. 7.

Figures 7a–7c show the effects of deflecting the aileron (indicated as A) by 1, 3, and 5 deg, respectively, while holding the flap (indicated as F) at 0 deg (no deflection) on the lift coefficient for $\alpha = 0$ to 25 deg. In a similar fashion, Figs. 7d–7f show the effects of deflecting the flap by 1, 3 and 5 deg, and Figs. 7g–7i show the effects of deflecting both the flap and aileron together by 1, 3, and 5 deg, respectively. No appreciable effects are observed in the aerodynamic forces for aileron deflection of 1 and 3 deg compared with the baseline case (see Figs. 7a and 7b). For aileron deflection of 5 deg, shown in Fig. 7c, a noticeable shift in the lift curve is observed for angles of attack up to 15 deg. This is the classical response of a plane flap that corresponds to an increase in the zero-lift angle of attack that is equivalent to an increase in the wing camber.

Comparisons between Figs. 7a and 7d, Figs. 7b and 7e, and Figs. 7c and 7f show that the effect of the inboard flap, which is smaller in size than the aileron, is stronger than the effect of the outboard aileron on the lift generated. Because the flow remains nominally attached at low angles of attack, the effects of the flap and aileron are considerably stronger than those with high angles of attack, at which flow separation and LEV become dominant. This limits the effectiveness of both the flap and aileron at high angles of attack. The maximum effect is observed when both the flap and aileron are deflected simultaneously (see Figs. 7g–7i). The lift augmentation effects of both control surfaces are roughly additive. In general, a linear shift in the lift coefficient corresponding to an increase in the zero-lift angle of attack is observed at low angles of attack by deflecting the flap/aileron, whereas at high angles of attack, their effects are nonexistent. Therefore, for flight control at higher angles of attack, conventional trailing-edge devices are not suitable. This is the basis for applying plasma actuators on the 1303 wing; that is, to demonstrate how the control authority can be greatly enhanced using a hingeless plasma flow control system.

The results from flow visualization tests conducted on a full-span wing model at $\alpha = 5$, 10, and 15 deg at $Re_c = 1.69 \times 10^5$ are shown in Fig. 8. The purpose of flow visualization tests was to was to understand the flow structure over the 1303 wing so that the locations of flow control actuators could be optimized to maximize their control effects. For the results shown in Fig. 8, fluorescent oil was used on the leeward surface of the wing to reveal the LEV and VBD patterns by capturing traces (streaklines) formed due to the viscous drag of the flow near the surface, after the model is placed in the test section for a certain length of time. A pair of leading-edge vortices is formed on the upper surface of the wing. The vortices are created by the rolling up of the shear layer that separates at the leading edge. The rotating flow reattaches to the surface and separates again to form a secondary vortex, evidenced in Fig. 8 (left) by the limiting streaklines (secondary separation). Leading-edge vortices are evident by the presence of secondary separation at $\alpha = 5$ deg, and no evidence of a VBD is observed. As the angle of attack is increased, the LEV bursts and results in a VBD. These VBD locations for $\alpha = 10$ and 15 deg are highlighted in Fig. 8. A comparison of $\alpha = 10$ and 15 deg photographs in Fig. 8 shows that the position of the VBD moves upstream as the angle of attack is increased. Above $\alpha = 15$ deg, VBD occurs over most of the wing. The secondary flow

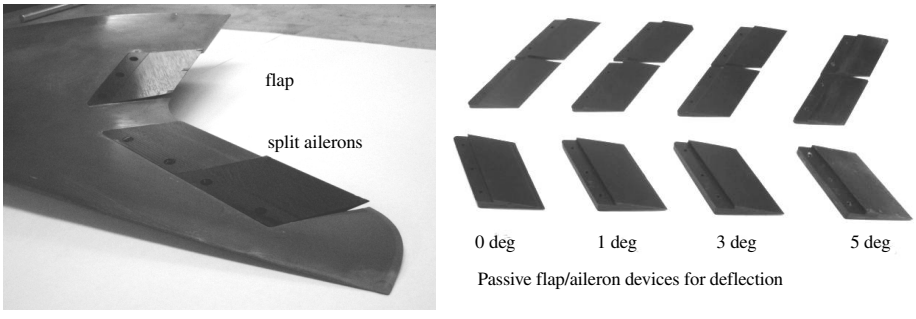

Fig. 6 Photographs showing the trailing edge of the wing model with conventional flap/aileron control surfaces.

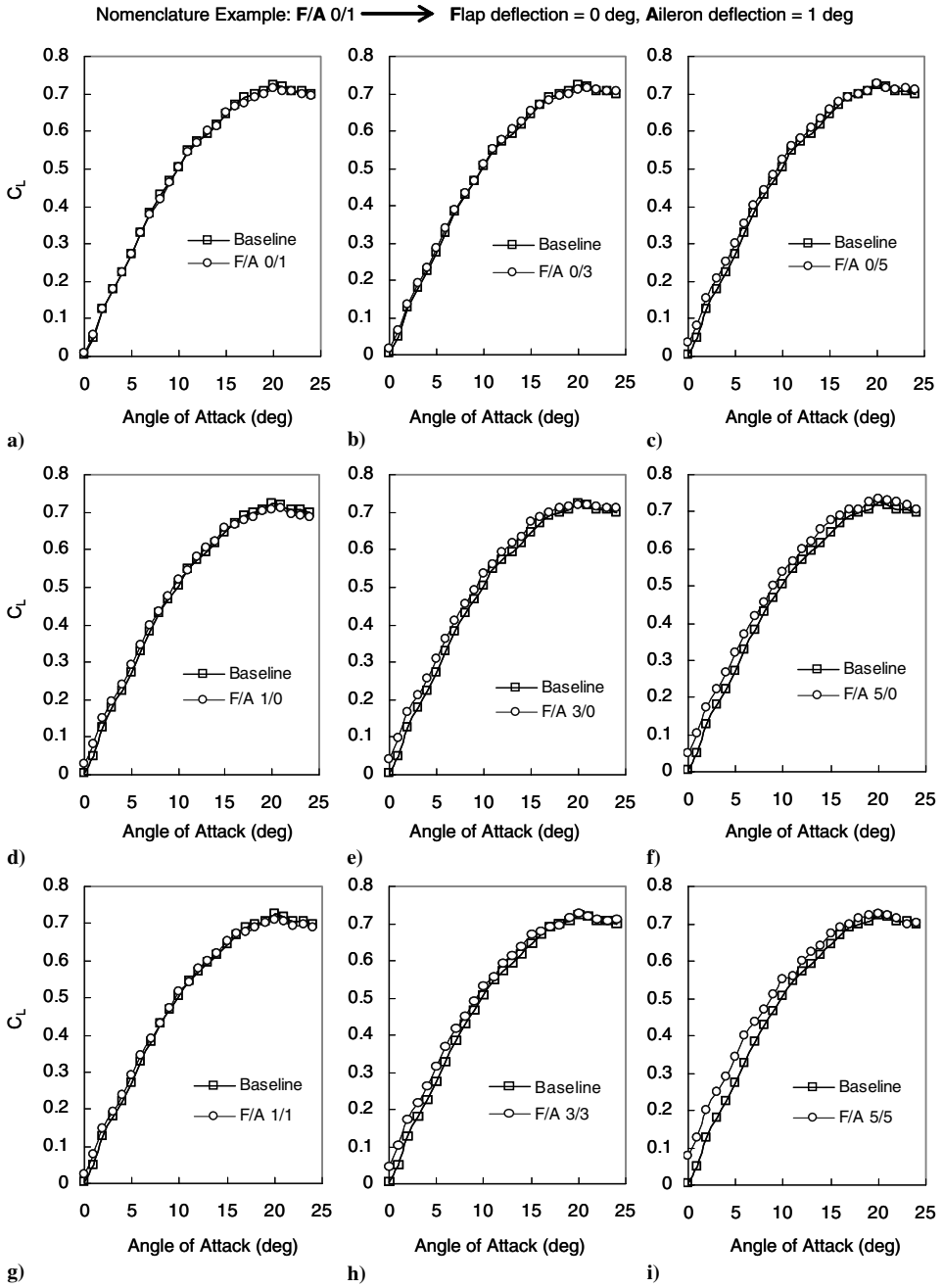

Fig. 7 Effects of a–c) deflecting aileron, d–f) flap, and g–i) both flap and aileron by 1, 3, and 5 deg, respectively, on the lift coefficient for $\alpha = 0$ to 25 deg.

that occur at high angles of attack explains the lack of effectiveness of the trailing-edge ailerons and flaps, documented in Fig. 7. In particular, the surface streaks show a large degree of flow separation and crossflow near the trailing edge, especially at the wingtips. This further explains why the ailerons were less effective than the inboard flaps.

The effect of the angle of attack on the LEV are further evidenced in Fig. 9, which presents photographs from laser-fluorescence flow visualization obtained at $\alpha = 5$, 10, and 15 deg (Figs. 9a–9c, Figs. 9d–9f, and Figs. 9g–9i, respectively) at multiple streamwise locations. These images focus on the large-scale vortex that scales with the wing half-span. They demonstrate that even after the VBD associated with the leading-edge separation vortex has occurred, the outer flow maintains a (weak) spiral behavior with an expanding core as it moves downstream in the wake of the wing. Figure 10 shows surface flow visualization results from a parallel study conducted on a half-span wing model, demonstrating similar LEV and VBD patterns to those in Fig. 8 on the leeward surface for different angles of attack. These surface visualizations capture more of the fine detail of the flow modules associated with the leading-edge flow separation and reattachment. At a 10-deg angle of attack, for example, they particularly highlight the primary vortex core and vortex at the wingtip. At 16 deg, the improvement in the visual information is substantially better than that shown in Fig. 8; this shows that the location of the breakdown of the primary vortex has moved inboard to approximately half of the wing span. The vortex at the wingtip is observed to have expanded to cover all of the region that would be occupied by an aileron.

The results from different plasma actuator experiments are presented in Figs. 11–15. Figures 11–13 highlight the results from the plasma actuator experiments conducted on the half-span wing model for achieving control at high angles of attack. The details of the specific plasma actuator configurations examined (e.g., P9, P10, P15, P18, and P19) are included in the captions for Figs. 11–13. In general, the letter P indicates a case with the plasma actuator on, and the number following P indicates a specific plasma actuator configuration, details of which are provided in the corresponding figure captions. Figures 11a–11f show the effects of P9, P10, and P15

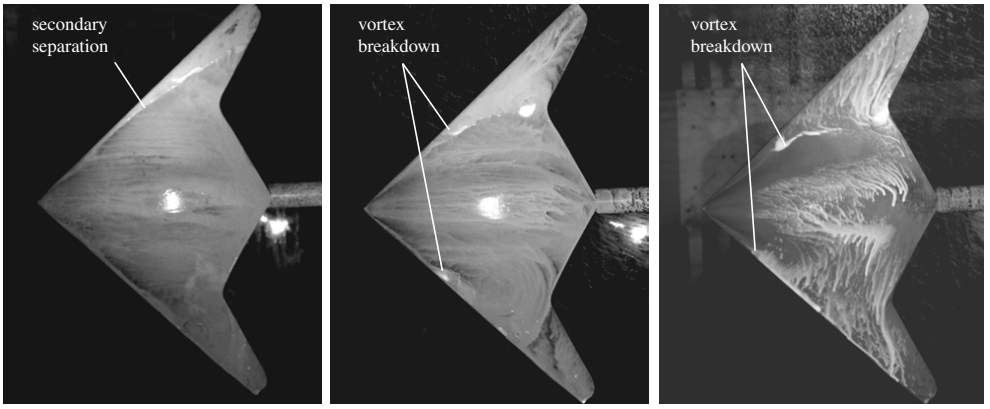

Fig. 8 Wind-tunnel flow visualization photographs of the lee side of a 47-deg swept wing with a blunt leading edge.

plasma configurations on the lift coefficient and drag polar, respectively, for angles of attack ranging from 0 to 35 deg. A comparison of the effects of P9, P10, and P15 with the baseline (B1/B4) reveals noticeable effects of the plasma actuators for $\alpha > 15$ deg, at which the VBD occupies most of the leading edge. There is negligible difference between the effects of P9 and P10 for all angles of attack tested (see Figs. 11a–11d), which suggests that the effects of plasma control on the leeward surface are similar for the inboard and outboard sections of the wing. However, Figs. 11c and 11f demonstrate a significant rise in the lift coefficient and a shift in the drag bucket, respectively. Plasma configuration P15 uses two unsteady actuators at the leading edge, slightly on the windward side. Studies have shown that at higher angles of attack, the primary separation location moves upstream, closer to the windward side of the wing, which seems to explain why P15 is more effective than P9 and P10.

Additional tests were conducted to verify this speculation and results from the new actuator configurations P18 and P19, which also used actuators slightly on the wind side. Results shown in Figs. 12 and 13 confirmed the effects of the leading-edge flow control observed earlier. Figure 14 summarizes the effects of the most promising plasma actuator configurations with the baseline case (no control) for α ranging from 0- to 35-deg angles of attack. At conditions in which the flow was nominally separated from the wing leading edge, the plasma actuators were able to produce significant control forces compared with those of the conventional trailing-edge flap/aileron. Effective control through the use of plasma actuators was observed through $\alpha = 15$ to 35 deg. Figure 15 shows a comparison of the plasma actuator effects with the conventional flap/aileron cases and the control-off case. This demonstrates the significant control forces that were generated using plasma actuators at high angles of attack.

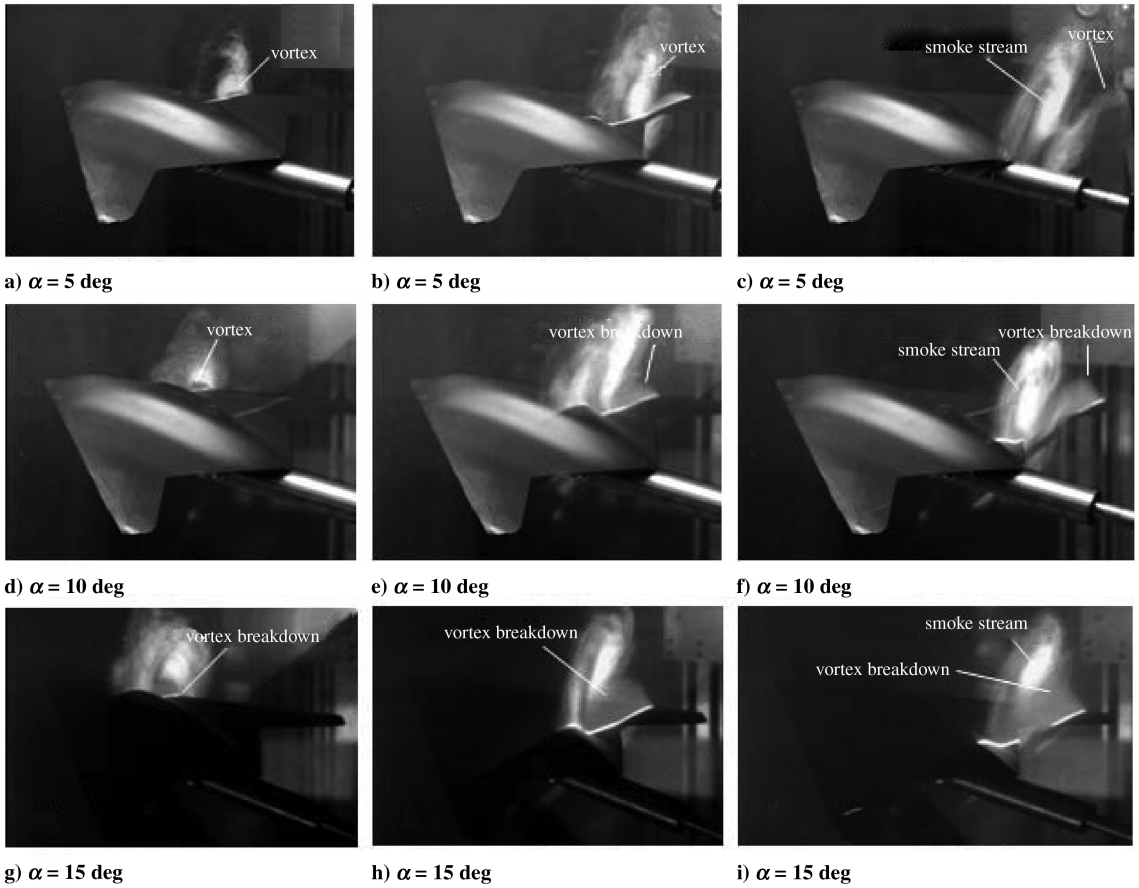

Fig. 9 Wind-tunnel flow visualization photographs of the lee side of a 47-deg swept wing with a blunt leading edge.

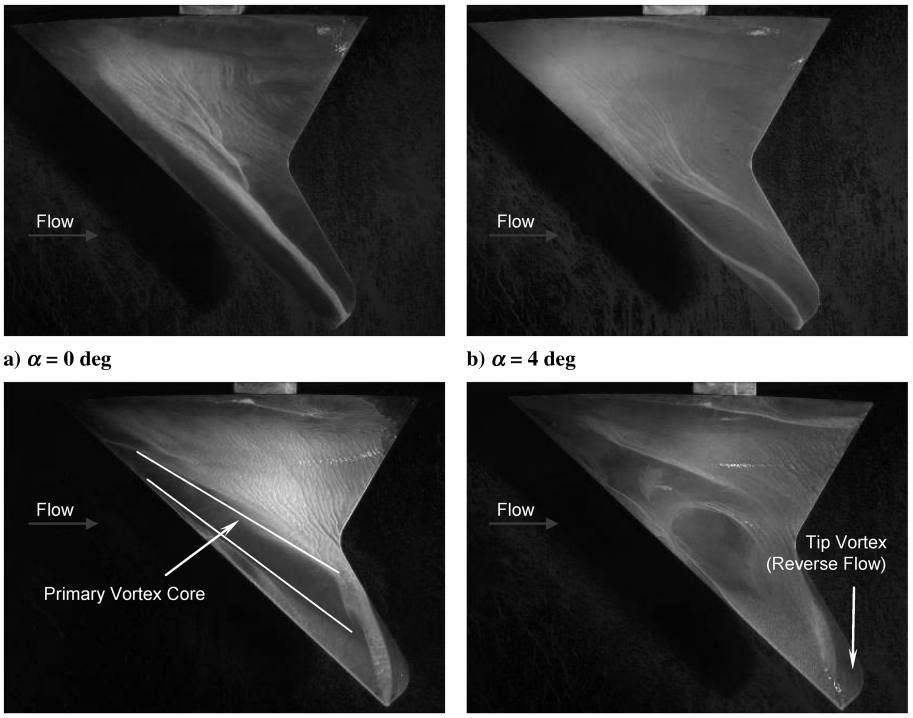

a) $\alpha = 0$ deg b) $\alpha = 4$ deg

c) $\alpha = 10$ deg d) $\alpha = 16$ deg

Fig. 10 Wind-tunnel flow visualization photographs of the lee side of a 47-deg swept wing with a blunt leading edge.

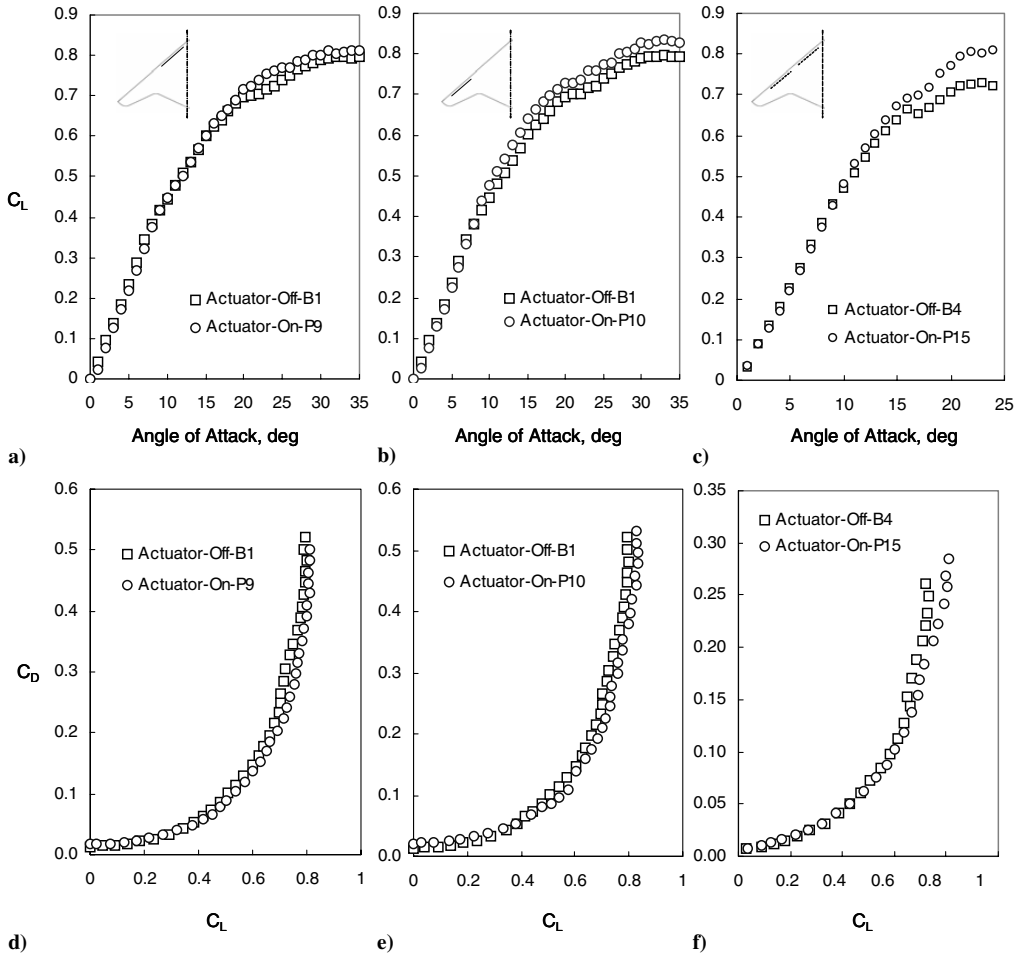

Fig. 11 Effects of plasma actuators on the lift coefficient (top) and drag polar (bottom) of the 47-deg swept wing for a range of angles of attack; P9: unsteady actuator located on the inboard section of the leading edge slightly on the lee side covering 40% of wing span; P10: unsteady actuator located at the outboard leading edge slightly on the lee side covering 40% of wing span; P15: a pair of unsteady actuators located at the inboard and outboard sections of the leading edge slightly on the wind side covering 80% of wing span.

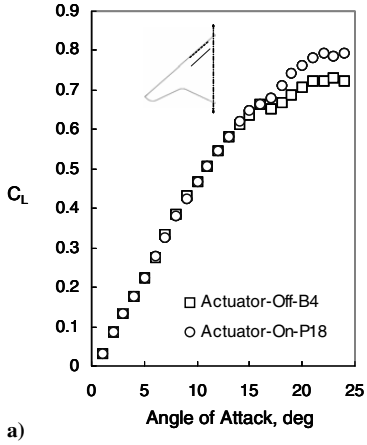

a)

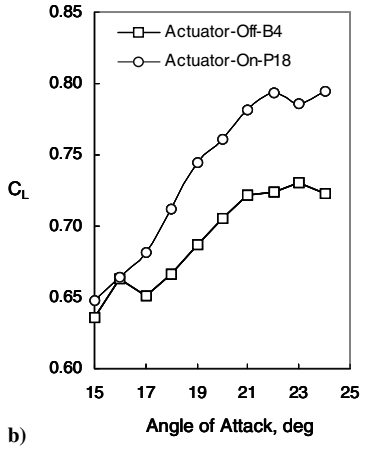

b)

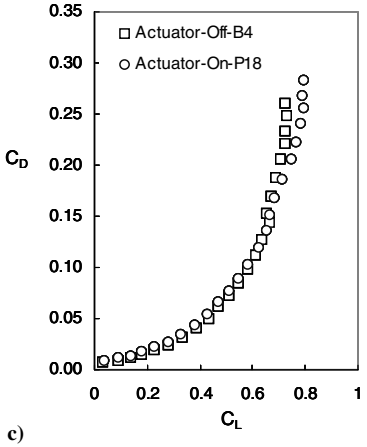

c)

Fig. 12 Effects of plasma actuators on the lift coefficient (top) and drag polar (bottom) of the 47-deg swept wing for a range of angles of attack; P18: a pair of unsteady plasma actuators on the inboard section (one on the wind side and the other on the lee side); B4: baseline.

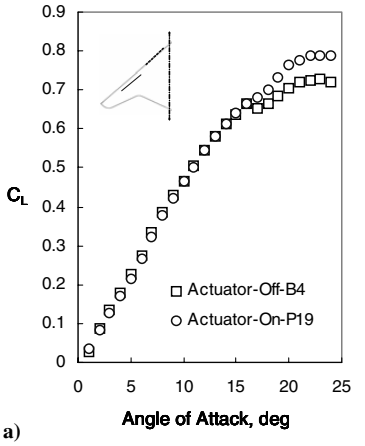

a)

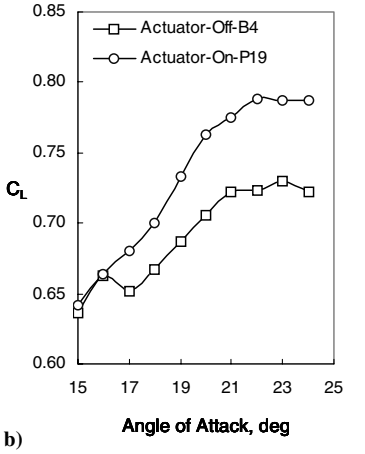

b)

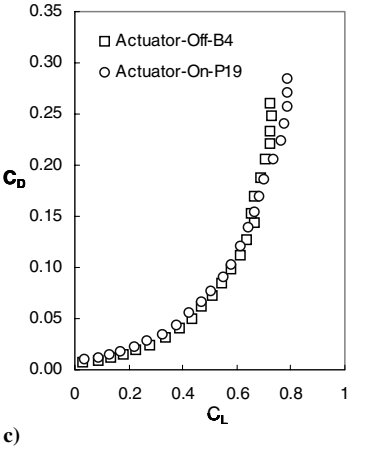

c)

Fig. 13 Effects of plasma actuators on the lift coefficient (top) and drag polar (bottom) of the 47-deg swept wing for a range of angles of attack; P18: a pair of unsteady plasma actuators on the inboard section (one on the wind side and the other on the lee side); B4: baseline.

IV. Conclusions

An experimental investigation was conducted to investigate the use of DBD plasma actuators for longitudinal control of a 1303 UCAV planform at high angles of attack with no moving surfaces. Control was implemented at the wing leading edge to provide longitudinal control without the use of hinged control surfaces. The concept employed the use of lee-side and wind-side plasma actuators at the wing leading edge to alter the aerodynamic lift and drag distributions over the 1303 planform by manipulating the flowfield over the lee side of the wing section. Data acquisition included force-balance measurements, laser fluorescence, and surface flow visualizations.

Flow visualization tests mainly focused on understanding the vortex breakdown phenomena over the baseline uncontrolled wing

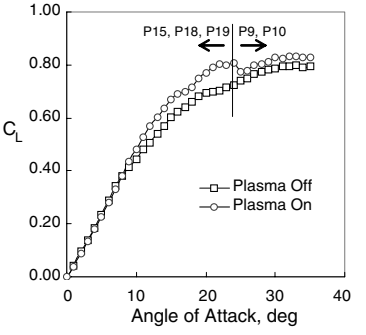

Fig. 14 Effects of unsteady plasma actuators on the lift coefficient at high angles of attack.

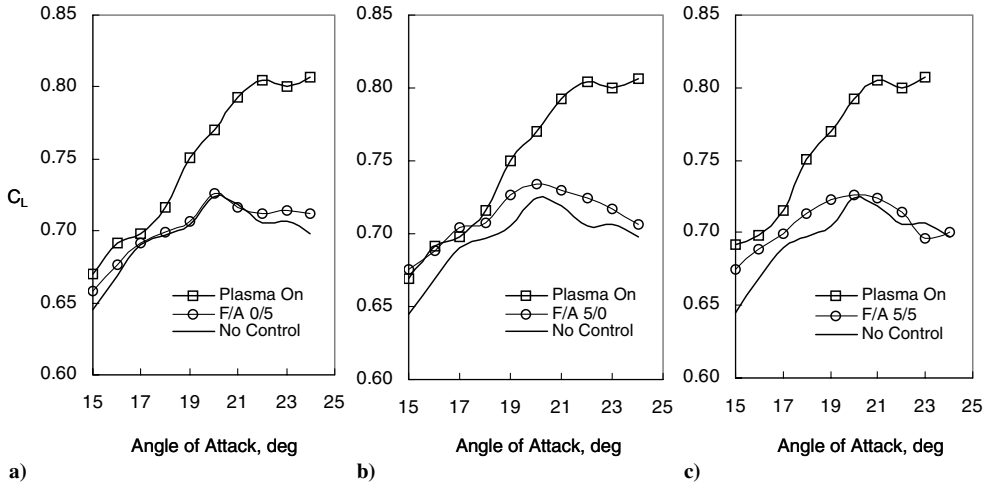

Fig. 15 Comparison of plasma effects with conventional control surfaces.

to aid in identifying optimal locations for plasma actuators for effective flow manipulation. The flow over the suction surface of a scaled 1303 UCAV model was found to be highly three-dimensional. Flow visualization of the lee side of the wing revealed complex flow patterns made up of three-dimensional leading-edge flow separation and vortices that swept over the wing at higher angles of attack. The primary vortex breakdown location progressively moved upstream over the wing as the angle of attack increased. This led to a complex flow that made conventional trailing-edge flaps and ailerons ineffective at angles of attack above 15 deg.

Force-balance results showed considerable changes in the lift and drag characteristics of the wing for the plasma-controlled cases compared with the baseline cases. When plotted with the effects of conventional trailing-edge devices, the plasma actuators demonstrated a significant improvement in the control authority and, therefore, the operational flight envelope of the wing. Optimum lift enhancement was achieved by placing the actuators at a chordwise location that was close to the leading edge on the suction side at $x/c \simeq 0.03$. The actuators were placed parallel to the leading edge and were operated in the unsteady mode to reduce power requirements to only 4 W per actuator span. For these, the actuator on the inboard half of the wing was only effective for angles of attack greater than 20 deg. The actuator on the outboard half of the wing was, however, effective for angles of attack from 9 deg up to the largest angle examined, 35 deg, for which the conventional trailing-edge flaps were ineffective. The results suggests that the application of plasma actuators on a swept UCAV planform can alter the flowfield of the leading-edge vortex in a manner that allows control without the use of hinged control surfaces. The study demonstrated the feasibility of a plasma wing concept for hingeless flight control of air vehicles.

Acknowledgments

This research was performed under a Phase 2 Small Business Innovation Research (SBIR) contract (no. FA8650-04-C-3405) issued by the U.S. Air Force Research Laboratory (AFRL). The authors would like to thank Charles F. Suchomel (AFRL program monitor), Carl P. Tilmann, and Roger Kimmel for their encouragement and support for this work.

References

[1] Gad-el-Hak, M., *Flow Control: Passive, Active, and Reactive Flow Management*, 1st ed., Cambridge Univ. Press, Cambridge, England, U.K., 2000.

[2] Klausmeyer, S. M., Papadakis, M., and Lin, J. C., "A Flow Physics Study of Vortex Generators on a Multi-Element Airfoil," AIAA Paper 96-0548, Jan. 1996.

[3] Patel, M. P., Carver, R., Ng, T. T., and Lisy, F. J., "Detection and Control of Flow Separation Using Pressure Sensors and Micro-Vortex Generators," AIAA Paper 2002-0268, Jan. 2002.

[4] Kruger, W., "Drag Reduction by Suction of the Boundary Layer Separated Behind Shock Wave Formation at High Mach Numbers," NACA TM 1168, July 1947.

[5] Tillman, T. G., and Hwang, D. P., "Drag Reduction on a Large-Scale Nacelle Using a Micro-Blowing Technique," AIAA Paper 99-0130, Jan. 1999.

[6] Sun, M., and Hamdani, H., "Separation Control by Alternating Tangential Blowing/Suction at Multiple Slots," AIAA Paper 01-0297, Jan. 2001.

[7] Corke, T., and Post, M., "Overview of Plasma Actuators: Concepts, Optimization, and Applications," AIAA Paper 2005-0563, Jan. 2005.

[8] Wie, D. M. V., Risha, D. J., and Suchomel, C. F., "Research Issues Resulting from an Assessment of Technologies for Future Hypersonic Aerospace Systems," AIAA Paper 2004-1357, Jan. 2004.

[9] Enloe, L., McLaughlin, T., VanDyken, R., Kachner, E., Jumper, Corke, T., Post, M., and Haddad., O., "Mechanisms and Response of a Single Dielectric Barrier Plasma Actuator: Geometric Effects," *AIAA Journal*, Vol. 42, No. 3, Mar. 2004, pp. 595–604.

[10] Enloe, L., McLaughlin, T., VanDyken, R., Kachner, E., Jumper, and Corke, T., "Mechanisms and Response of a Single Dielectric Barrier Plasma Actuator: Plasma Morphology," *AIAA Journal*, Vol. 42, No. 3, Mar. 2004, pp. 589–594.

[11] Orlov, D. M., Corke, T. C., and Patel, M. P., "Electric Circuit Model for the Aerodynamic Plasma Actuator," AIAA Paper 2006-1206, Jan. 2006.

[12] Corke, T., Cavalieri, D., and Matlis, E., "Boundary Layer Instability on a Sharp Cone at Mach 3.5 with Controlled Input," *AIAA Journal*, Vol. 40, No. 5, 2001, p. 1015.

[13] Corke, T., Jumper, E., Post, M., Orlov, D., and McLaughlin, T., "Application of Weakly Ionized Plasmas as Wing Flow-Control Devices," AIAA Paper 2002-0350, Jan. 2002.

[14] Huang, J., Corke, T., and Thomas, F., "Plasma Actuators for Separation Control of Low-Pressure Turbine Blades," AIAA Paper 2003-1027, Jan. 2003.

[15] Post, M., and Corke, T., "Separation Control on High Angle of Attack Airfoil Using Plasma Actuators," *AIAA Journal*, Vol. 42, No. 11, Jan. 2004, pp. 2177–2184.

[16] Corke, T. C., and Matlis, E., "Phased Plasma Arrays for Unsteady Flow Control," AIAA Paper 2000-2323, June 2000.

[17] Post, M., and Corke, T., "Separation Control Using Plasma Actuators—Stationary and Oscillating Airfoils," AIAA Paper 2004-0841, Jan. 2004.

[18] Corke, T., He, C., and Patel, M. P., "Plasma Flaps and Slats: an Application of Weakly Ionized Plasma Actuators," AIAA Paper 2004-2127, June 2004.

[19] Patel, M. P., Sowle, Z. H., Corke, T. C., and He, Chuan, "Autonomous Sensing and Control of Wing Stall Using a Smart Plasma Slat," *Journal of Aircraft*, Vol. 44, No. 2, Mar.–Apr. 2007, pp. 516–527.

[20] Corke, T. C., Mertz, B., and Patel, M. P., "Plasma Flow Control Optimized Airfoil," AIAA Paper 2006-1208, Jan. 2006.

[21] Rao, D. M., and Johnson, T. D., "Alleviation of the Subsonic Pitch-Up of Delta Wings," *Journal of Aircraft*, Vol. 20, No. 6, June 1983, pp. 530–535.

[22] Lee, M., and Ho, C. M., "Vortex Dynamics of Delta Wings," *Frontiers in Experimental Fluid Mechanics*, Lecture Notes in Engineering, Springer–Verlag, Berlin, Vol. 46, 1989, pp. 365–427.

[23] Visser, K. D., and Nelson, R. C., "Measurements of Circulation and Vorticity in the Leading-Edge Vortex of a Delta Wing," *AIAA Journal*, Vol. 31, No. 1, Jan. 1993, pp. 104–111.
[24] Visser, K. D., Ferrero, M., and Nelson, R. C., "Physical Considerations of Leading-Edge Flows," AIAA Paper 2004-5083, Aug. 2004.
[25] Moeller, E. B., and Rediniotis, O. K., "Hingeless Flow Control over a Delta Wing Platform," AIAA Paper 2000-117, Jan. 2000.
[26] Amitay, M., Washburn, A. E., Anders, S. G., and Parekh, D., "Active Flow Control on the Stingray Uninhabited Air Vehicle: Transient Behavior," *AIAA Journal*, Vol. 42, No. 11, Nov. 2004, pp. 2205–2215.
[27] Visser, K. D., "An Investigation of the Effects of an External Jet on the Performance of a Highly Swept Delta Wing," M.S. Thesis, Univ. of Notre Dame, Notre Dame, IN, 1988.
[28] Visser, K. D., Nelson, R. C., and Ng, T. T., "A Flow Visualization and Force Data Evaluation of Spanwise Blowing on Full and Half Span Delta Wings," AIAA Paper 89-0192, Jan. 1989.
[29] Visser, K. D., Iwanski, K. P., Nelson, R. C., and Ng, T. T., "Control of Leading Edge Vortex Breakdown by Blowing," AIAA Paper 88-0504, Jan., 1988.
[30] Zhang, F., Khalid, M., and Ball, N., "A CFD Based Study of UCAV 1303 Model," AIAA Paper 2005-5615, June 2005.
[31] Nelson, R., Corke, T. C., He, C., Otham, H., Matsumo, T., Patel, M. P., and Ng, T. T., "Modification of the Flow Structure over a UAV Wing for Roll Control," AIAA Paper 2007-884, Jan. 2007.
[32] Lopera, J., Ng, T. T., Patel, M. P., Vasudevan, S., and Corke, T. C., "Aerodynamic Control of 1303 UAV Using Windward Plasma Actuators on a Separation Ramp," AIAA Paper 2007-0636, Jan. 2007.
[33] Wong, M., McKenzie, G., Ol, M., Petterson, K., Zhang, S., "Joint TTCP CFD Studies into the 1303 UCAV Performance: First Year Results," AIAA Paper 2006-2984, June 2006.
[34] S. McParlin, S., Bruce, R., Hepworth, A., and Rae, A., "Low Speed Wind Tunnel Tests on the 1303 UCAV Concept," AIAA Paper 2006-2985, June 2006.
[35] Petterson, K., "Low-Speed Aerodynamic and Flowfield Characteristics of a UCAV," AIAA Paper 2006-2986, June 2006.
[36] Wong, M., and Flores, J., "Application of OVERFLOW-MLP to the Analysis of the 1303 UCAV," AIAA Paper 2006-2987, June 2006.
[37] Milne, M., and Arthur, M., "Evaluation of Bespoke and Commercial CFD Methods for a UCAV Configuration," AIAA Paper 2006-2988, June 2006.